



Design of a sustainable prepolarizing magnetic resonance imaging system for infant hydrocephalus

Johnes Obungoloch^{1,2,3} · Joshua R. Harper^{1,4} · Steven Consevage^{1,5} · Igor M. Savukov⁶ · Thomas Neuberger^{2,7} · Srinivas Tadigadapa⁸ · Steven J. Schiff^{1,2,4,5,9}

Received: 3 December 2017 / Revised: 11 March 2018 / Accepted: 15 March 2018
© ESMRMB 2018

Abstract

Objectives The need for affordable and appropriate medical technologies for developing countries continues to rise as challenges such as inadequate energy supply, limited technical expertise, and poor infrastructure persist. Low-field magnetic resonance imaging (LF MRI) is a technology that can be tailored to meet specific imaging needs within such countries. Its low power requirements and the possibility of operating in minimally shielded or unshielded environments make it especially attractive. Although the technology has been widely demonstrated over several decades, it is yet to be shown that it can be diagnostic and improve patient outcomes in clinical applications. We here demonstrate the robustness of prepolarizing MRI (PMRI) technology for assembly and deployment in developing countries for the specific application to infant hydrocephalus. Hydrocephalus treatment planning and management requires only modest spatial resolution, such that the brain can be distinguished from fluid—tissue contrast detail within the brain parenchyma is not essential.

Materials and Methods We constructed an internally shielded PMRI system based on the Lee-Whiting coil system with a 22-cm diameter of spherical volume.

Results In an unshielded room, projection phantom images were acquired at 113 kHz with in-plane resolution of 3 mm × 3 mm, by introducing gradient fields of sufficient magnitude to dominate the 5000 ppm inhomogeneity of the read-out field.

Discussion The low cost, straightforward assembly, deployment potential, and maintenance requirements demonstrate the suitability of our PMRI system for developing countries. Further improvement in image spatial resolution and contrast of LF MRI will broaden its potential clinical utility beyond hydrocephalus.

Keywords Hydrocephalus · Prepolarization MRI · Low field · Ultra-low field

✉ Steven J. Schiff
sschiff@psu.edu

¹ Center for Neural Engineering, The Pennsylvania State University, University Park 16802, USA

² Department of Biomedical Engineering, The Pennsylvania State University, University Park 16802, USA

³ Mbarara University of Science and Technology, P.O. Box 1410, Mbarara, Uganda

⁴ Department of Engineering Science and Mechanics, The Pennsylvania State University, University Park 16802, USA

⁵ Department of Physics, The Pennsylvania State University, University Park 16802, USA

⁶ Los Alamos National Laboratory, Los Alamos 87545, USA

⁷ The Huck Institutes of the Life Sciences, The Pennsylvania State University, University Park 16802, USA

⁸ Department of Electrical Engineering, The Pennsylvania State University, University Park 16802, USA

⁹ Department of Neurosurgery, Penn State College of Medicine, Hershey 17033, USA

Introduction

Hydrocephalus is the most common condition in children world wide that requires brain imaging and neurosurgical treatment. It is estimated that there are as many as 200,000 new cases of hydrocephalus per year throughout sub-Saharan Africa (SSA) alone [1]. In SSA, most cases can be postinfectious, which increases the need for structural imaging to guide treatment, since bacterial brain infections can lead to substantially increased complexity of the fluid spaces within the brain [2]. The cost-effectiveness of treating infant hydrocephalus in SSA, with appropriate imagery, has been well demonstrated [3]. Furthermore, it has recently been demonstrated in African infants that measuring brain volume on imaging can provide useful metrics of brain growth arrest with increased intracranial pressure prior to treatment, and catch-up growth in infants who do well cognitively following successful relief of pressure after surgery [4].

Hydrocephalus in infancy also presents one of the most straightforward challenges for magnetic resonance imaging (MRI). In these cases, the most important task is to segment an image into brain and cerebrospinal fluid (CSF). Rooney et al. found that at 0.2 T, the T1 for CSF, white matter, and grey matter are, respectively, 4.42 s, 361 ms, and 636 ms [5]. This makes segmentation between brain tissue and CSF straightforward. The requirements for tissue contrast within the brain, or grey and white matter discrimination, are not important for diagnostics and treatment of hydrocephalus. Similarly, the spatial resolution required to affect treatment decisions are low—fluid compartments of at least multiple cubic centimeters in volume must be identified for fenestration or drainage. Although almost all new cases are seen in infancy, a hydrocephalic child's head can readily grow to adult size early within the first year of life. On the other hand, the small infant body permits design of imaging systems far smaller than that required for adult imaging.

MRI is arguably the safest technology for brain imaging to diagnose hydrocephalus, but it is also the most expensive structural brain imaging modality available. Conventional high-field (HF) MRI uses very strong magnetic fields generated by superconducting magnets. Additionally, fringe fields from HF MRI systems must be shielded, adding cost for the system. The high cost, typically US \$1 million per Tesla for whole-body cryogenic MRI scanners [6], high power requirements, stringent technical demands, and strict infrastructure specifications have hindered the proliferation of HF MRI in developing countries. As a less expensive option, developing countries more often use computed tomography (CT) for brain imaging [7]. While this alleviates many of the financial and infrastructure difficulties of HF MRI, CT contains components that are expensive to service and maintain in the developing world and delivers relatively high doses of

ionizing radiation, a particular hazard to infants [8]. It is our position that the high tissue contrast and fine spatial resolution provided by typical CT or HF MRI substantially exceed what is required to reach surgical management decisions and achieve good patient outcomes in hydrocephalus.

LF coil-based MRI systems can offer an affordable, sustainable, and safe alternative to HF MRI and CT for brain imaging in developing countries by reducing costs in both materials and manufacturing, lowering power requirements, eliminating the need for specialized equipment siting, and simplifying the technical aspects of troubleshooting, operation, and repair. The practicality of LF MRI was recognized from the inception of MRI technology in the 1980s. In 1985, for example, Sepponen et al. studied cerebral lesions using static LF MRI with a main field (B_0) of 20 mT and established considerable contrast between lesions and other brain tissues [9]. Nascimento et al. demonstrated whole-brain imagery with a low-cost system at 16 mT using a novel digital transmit–receive system [10]. The introduction of prepolarizing MRI (PMRI) technology by Conolly and colleagues in 1993 expanded the potential benefits offered by LF MRI technology [11]. PMRI uses two separately optimized electromagnet systems to provide a weak static and homogeneous magnetic field (B_m) at which the image is acquired and a relatively strong pulsating magnetic field (B_p) to provide additional polarization before image acquisition. This technique allows acquisition of MR signal at very low frequencies provided by the B_m field while taking advantage of the high signal-to-noise ratio (SNR) provided by the B_p field. Other advantages of this technology include low power requirements and relaxation of the magnetic field homogeneity requirements for the stronger B_p field [11]. Using this technique, Conolly et al. acquired an image of a human hand with remarkable resolution and contrast using a B_m field of 57 mT and B_p field of 0.4 T [12]. Similarly, with a reduced field strength of 2 mT for B_m and a prepolarizing field of 0.1 T, Savukov et al. performed imaging of the human hand [13] and partial imaging of the adult head [14].

PMRI is not the only LF MRI technology that could be appropriate for developing countries, and it has its challenges. Rapidly ramping up the B_p is challenging, as it requires high intermittent power and introduces eddy currents into the system. Furthermore, there is strong induction coupling between the B_p and B_m , which can negate the advantage gained by using B_p . Therefore, other methods of LF and sustainable imaging are under development. Recently, there have been demonstrations of imaging using static LF MRI systems that also show promise. Lothar et al. developed a novel design of a Helmholtz coil-based MRI system in which steel plates were used to boost the magnetic field within the coil arrangement and simultaneously shield the system from electromagnetic interference [15]. With a field strength of 23 mT and a field of view (FOV) of 10 cm

diameter of spherical volume (DSV), an image with in-plane resolution of 1.6 mm × 1.6 mm was acquired in 19 min. The system operates at 500 W. Similarly, Sarracanie et al. used a novel Helmholtz coil-based LF system to acquire images of the human brain [16]. Working with a 6.5-mT main magnetic field generated using 220-cm diameter Helmholtz coils, images were acquired in 6 min with in-plane resolution of 2.5 mm × 3.5 mm.

Permanent magnet MRI systems, particularly Halbach arrays, are another type of LF MRI with possible applications in developing countries. Halbach arrays were introduced in 1980 when Klaus Halbach developed a method of cylindrically arranging small permanent magnets to generate uniform magnetic fields [17]. This method allows for construction of relatively low-weight permanent magnet MRI systems. Kimura et al. developed a Halbach array MRI system and used it for outdoor imaging of tree branches in 2011 [18]. However, because of the difficulty of creating gradient magnetic fields, mechanical rotation and translation of the system was required for slice selection and imaging. Meanwhile, Kose and Haishi added gradient magnetic fields from electromagnets to a permanent magnet system and acquired 2D images without the need for rotation and translation [19]. More recently, Cooley et al. used a Halbach array to acquire 2D phantom images without the use of gradients [20]. Their Halbach system had a field strength of 77.3 mT and a 16-cm FOV.

While Halbach array systems are attractive because of their low power requirement, it is challenging to generate uniform magnetic fields in large-bore systems [21]. Additionally, slice selection and 3D imaging using Halbach arrays compounds design complexity by requiring mechanical rotations and translations or powered electromagnets to produce gradient fields. Static magnet LF MRI systems, on the other hand, require more continuous power than PMRI systems. Helmholtz design of static magnet MRI systems are especially power demanding. To generate a homogeneous magnetic field over the FOV large enough to accommodate an adult head, the Helmholtz coils must be at least several meters in diameter [22]. The current required to generate a magnetic field of 1 mT at the center of such a coil system would be 1100 Ampere-turns. The same field could be generated using Lee-Whiting coil arrangement with diameter of 0.5 m, requiring only 28 Ampere-turns [23]. Furthermore, for very low readout fields, the SNR of PMRI is proportional to the product of B_p and the square root of B_m fields. For relatively higher readout fields >23 mT, the SNR becomes proportional to only B_p . Therefore, the SNR of a PMRI system can be comparable with that of static MRI systems, where B_0 is equal to B_p [11], provided the inductive effects of B_p coil switching are eliminated. In this way, generating a small static magnetic field (B_m) while periodically switching to the stronger magnetic field (B_p) saves power and mitigates heating while matching SNR capabilities of static-field LF MRI systems. For these reasons, we designed a PMRI

system for our introduction into a developing country context. We modified and redesigned the PMRI system from [14] to accommodate a 22-cm DSV FOV and operate at 550 W. The B_m field was generated by a Lee-Whiting coil arrangement, the B_p field was generated by a solenoid, while the longitudinal gradient field was generated by a Maxwell coil pair and transverse gradients by Golay coils.

RF coils were saddles capable of accommodating an adult human head. We demonstrated the feasibility of using this PMRI system by imaging a variety of test phantoms with only internal shielding within the device.

Materials and methods

PMRI coils

Coil configuration of the PMRI system includes the B_m coil, B_p coil, gradient coils, and radio frequency (RF) coils. These are described in the methodology below.

The B_m coil

In designing the B_m coil, homogeneity of the magnetic field is a major factor to consider. Magnetic field inhomogeneities introduce artifacts that degrade the quality of the resulting image. A number of coil designs, including the Merritt three-, four-, and five-coil systems [24], the Rubens five-coil system [25], the Helmholtz and Lee-Whiting coil system [23], among others, have been shown to generate acceptable field homogeneities. Of these, the Lee-Whiting coil system is relatively easy to implement and produces sufficiently homogeneous magnetic fields over large volumes [26]. Magnetic field homogeneity requirements for LF MRI systems vary between researchers, but Lothar et al. generated acceptable images with magnetic field homogeneities of 1200 ppm over a 10-cm DSV [15]. The Lee-Whiting coil system consists of two coil pairs symmetrically positioned from the center along the z -axis [23], with Ampere turn ratios of 9:4:4:9. Using the Biot–Savart law, the magnetic field B_z along the axis of the Lee-Whiting coil system is given by

$$B_z = \frac{9\mu_0 n I a^2}{2(a^2 + (z - s_1))^{3/2}} + \frac{4\mu_0 n I a^2}{2(a^2 + (z - s_2))^{3/2}} + \frac{4\mu_0 n I a^2}{2(a^2 + (z + s_2))^{3/2}} + \frac{9\mu_0 n I a^2}{2(a^2 + (z + s_1))^{3/2}} \quad (1)$$

where n is the number of turns, a is the radius of the coil system, I is the current in the coils, s_1 and s_2 are positions of the inner and outer coils, respectively, from the center along the axis of the coil arrangement, and μ_0 is permeability of

free space. The field at the center ($z=0$) is $\approx 17.96/D$ $\mu\text{T}/\text{A}$ for a single turn [23], where D is the diameter of the coil arrangement.

In our design of the B_m system, a power requirement of 500 W at 10 A, and 5- Ω resistance was imposed as a design constraint. Coil selection was based on power restrictions and wire size. The wire length was determined by resistance.

Enameled copper wire with nominal diameter of 2.07 mm and resistance of 2.315×10^{-3} Ω/m was used [27]. The length of the conductor was calculated to be 940 m. The Lee-Whiting coil system was then wound with outer coils, having 207 turns and the inner coils having 92 turns. The diameter of the Lee-Whiting coil system was 47.5 cm. The axial separation of the inner and outer coils were ± 5.8 and ± 22.3 cm, respectively, from the center of the coil system. COMSOL, a finite element analysis and solver software, was used to simulate the theoretical level of magnetic field homogeneity achievable for the given dimensions of the coil. COMSOL calculates a map of the static magnetic field using the Ampere's equation

$$\nabla \times H = J \quad (2)$$

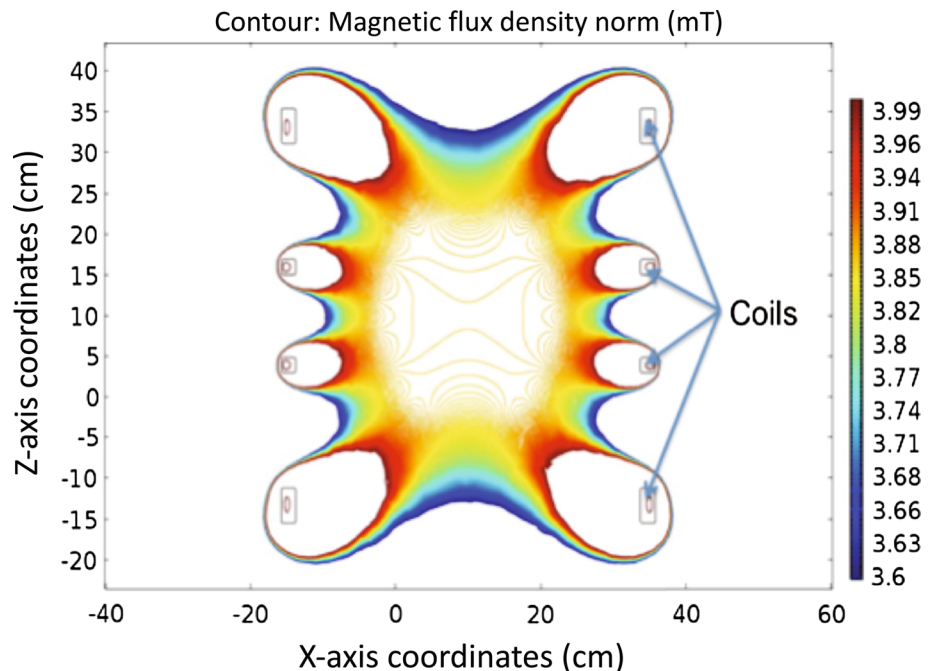
where H is the magnetic flux density and J is the current density, from which the static magnetic field B is given as $B = \nabla \times A$ and $H = \mu B$, where A is the magnetic vector potential, and μ is the permeability of the material. The generated profile of the magnetic field is shown in Fig. 1.

B_p magnet coil

In PMRI systems, magnetic field inhomogeneities of up to 30% for the B_p coil are considered acceptable, as such non-uniformity leads to changes in image brightness of the image [11], which can be corrected numerically. The B_p magnet coil was therefore constructed as a simple solenoid coil that produces relatively large magnetic fields for a given copper mass and provides sufficient field uniformity. The maximum power requirement was set at 500 W. A cylindrical aluminum tube with inner diameter of 30 cm and outer diameter of 30.8 cm was used as the coil-supporting structure. Wire size was determined to be 2.6 mm in diameter, wire length was 1525 m based on power requirements, and coil resistance was calculated to be 5 Ω . The required number of turns as calculated from wire length and tube diameter would be 1576 turns.

To construct a solenoid coil with field inhomogeneity within 30% over the FOV of 25 cm in length, dimensions were optimized with the COMSOL model by varying the length of the solenoid from 25 to 45 cm in steps of 5 cm while the magnetic field strength along the axis was evaluated. It was observed that while magnetic field homogeneity of the solenoid improved with increasing length, magnetic field strength was reduced. The optimized B_p coil was wound as a solenoid of 40-cm long, inner diameter 30 cm, and outer diameter 38 cm. The number of turns was 1188, actual solenoid resistance was 3.5 Ω , and inductance of 40 mH giving a time constant of 50 ms. The average field strength over the length of the solenoid was 3.7 mT/A.

Fig. 1 COMSOL simulation contour plot of the B_m field homogeneity on the center xz -plane. The inner coils of the Lee-Whiting system had 92 turns each and the outer coils had 207 each. A direct current of 4.71 A was injected into the coils. The *contour lines* are 10- μT apart. Mean field at the center was 3.875 mT. B_m field inhomogeneity over a 22-cm diameter was 1300 ppm



Gradient coils

Gradient coils were based on standard designs. The Z-gradient was made from a Maxwell coil pair 25.53 cm in radius. Coil separation for the z-gradient was 44.72 cm. Maxwell coils with such specifications give a uniform and linear magnetic field to a spherical region defined by a radius of $\frac{1}{2}R$ [28]. This is a large enough region for our purpose given the radius of our coils. The transverse gradients were constructed as Golay coils [29] with a diameter of 54.5 cm, inner arc separation of 21.25 cm, and outer arc separation of 68 cm. Litz wire was used for the gradient coils rather than single stranded copper wire to make it smoother to wind around sharp corners as required in making Golay coils.

RF coils

We used two separate RF coils—one as the transmit coil and the other as the receiver coil. We considered two major parameters when designing both RF coils—the resonant frequency and the quality factor. Both RF coils were saddle coils with length to diameter ratio of 1.2. The receiver coil had a diameter of 22 cm and arc angle of $\sim 120^\circ$. The saddle wire packs comprised ten turns of a 105-strand 1.29-mm Litz wire. High Q-factor ceramic capacitors with values ranging between 1 and 5 nF were used to tune the coil to frequencies between 100 and 300 kHz. The transmit coil had a diameter of 27 cm and an arc angle of $\sim 120^\circ$. Saddle wire packs had four turns of 105 strands of Litz wire with nominal diameter of 1.29 mm. Interaction between coils was minimized by orienting them in such a way that their magnetic fields were orthogonal to each other. A SR560 low-noise-voltage preamplifier from Stanford Research Systems was used for the receive coil, and a home-built RF amplifier based on a OPA 134 Op-amp configuration was used for the transmit coil.

RF shield

The imaging volume of the PMRI system was partially shielded using an open-ended cylindrical aluminum shield. An aluminum sheet 0.8128-mm thick was formed into a cylinder of 28.5 cm in diameter and 61 cm in length. Skin depth δ of a material is given by [30]

$$|\delta| = \sqrt{\frac{2\rho}{\mu\omega}}, \quad (3)$$

where ρ is the resistivity of the material, μ is permeability, and ω is frequency.

Our system is designed to work between 100 and 300 kHz, and skin depth for aluminum at these frequencies is

much smaller than the thickness of the shield. Theoretically, electromagnetic interference is shielded by absorption and reflection, and the shielding effectiveness (SE) of a material is given by [31],

$$SE(\text{dB}) = 20 \log \frac{\eta_o}{4\eta} + 20 \frac{x}{\delta}, \quad (4)$$

where η_o is the wave impedance of air and η is the wave impedance of the material, x is the material thickness, and δ is skin depth of the material. Shielding effectiveness for the open-ended aluminum shield at our frequency of operation, calculated based on [32], was 34 dB. The grounding terminal welded onto the shield was connected to the electrical ground of the building through the power outlet. The eddy currents within the shield must decay faster than coil transients, because with the chosen delay in the $\pi/2$ pulse, we do not observe significant effects of eddy currents. A small hole at one end of the shield permitted entry of magnet, gradient, and RF wires to the respective coils.

Magnet coil assembly

Following the procedures described above, the PMRI system was finally wound by hand and assembled starting with the receiver coil as the inner-most coil, the transmit coil, the B_p coil, the B_m , the Z-gradient coil, and X and Y gradients as the outer most coils as shown in Fig. 2. The system consists of coils described in the methods section and is mounted on a wooden frame. The overall length of the system is 67 cm and the internal diameter is 22 cm. The system, which includes the coil system and housing, weighs 125 kg

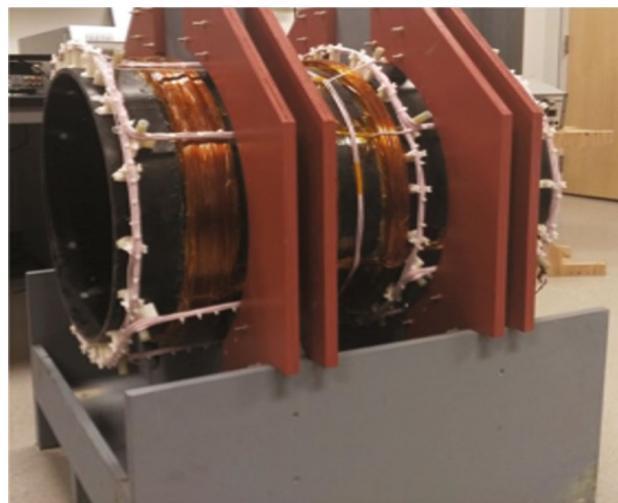


Fig. 2 PMRI coil system after construction and assembly, mounted on a wooden frame. Gradient coils are seen as white circular rings and the B_m coils are visible as brown rings

and costs \$18,000 in materials. The electronic components which included power supplies, gradient and signal amplifiers costs roughly \$12,000. The control system was implemented in LabView and the cost of developing the LabView code is not included here.

Results

After construction of the PMRI system, homogeneity and linearity of the magnetic fields generated by the B_m and gradient coils were evaluated, and imaging experiments were performed.

B_m field homogeneity

The magnetic field inside the PMRI system was mapped using a gaussmeter (DSP 475, Lake Shore, USA). The gaussmeter probe was mounted on the Z-axis of an in-house-built three-axis manipulator capable of adjustments to a precision of 2 mm. The B_m coil was energized by injecting a current of 4.71 A at 22 V using a DC power supply (Xantrex XDL 35-5 T, USA). Measurements were taken at 1-cm intervals over a volume of 16 cm \times 16 cm \times 16 cm. Results were processed in MATLAB to generate the magnetic field map showing homogeneity of the B_m magnetic field. MATLAB contour plots showing magnetic field homogeneity on the xy -plane at $z = 1$ cm and $z = -11$ cm are shown in Fig. 3.

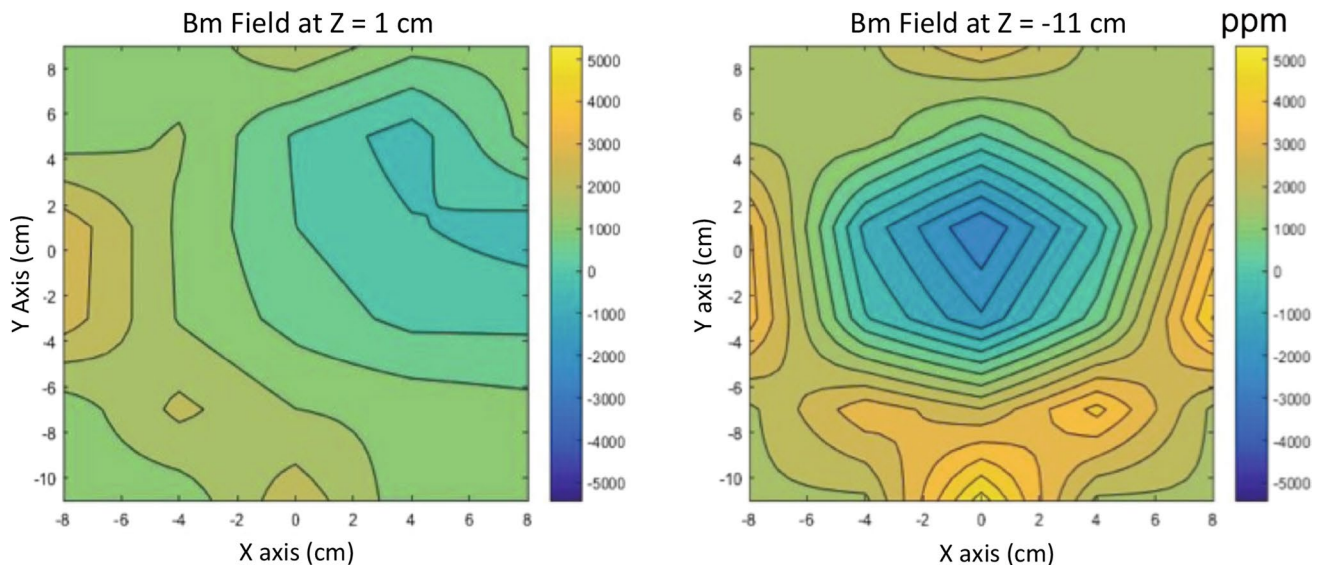


Fig. 3 B_m magnetic field homogeneity on the XY plane at $z = 1$ cm (left) and $z = -11$ cm (right). Contour lines are 500 ppm. Scale bar is in parts per million (ppm), and the mean field strength is 4 mT. The center of the system is at $z = 0$

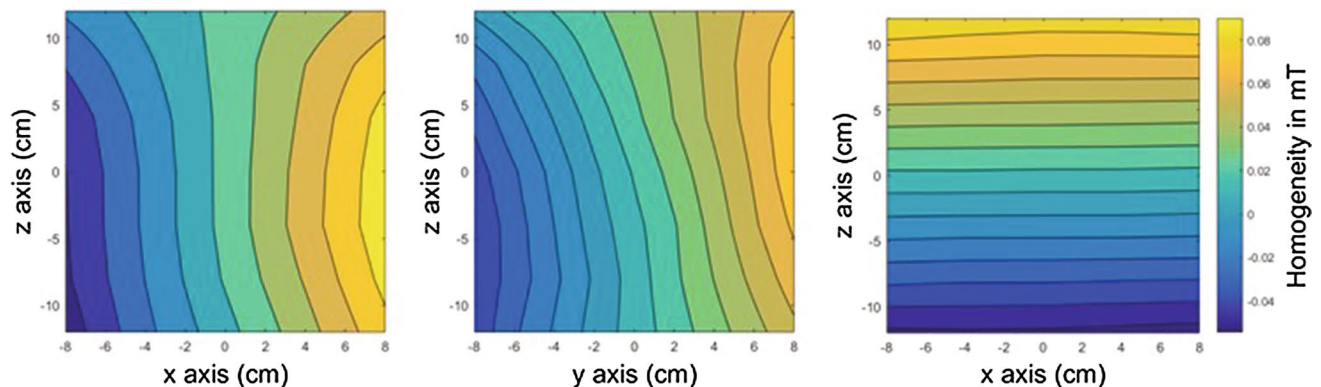


Fig. 4 Contour plots of magnetic field uniformity for the X, Y, and Z gradients. Contour lines are 10- μ T apart. Curvature of the contour lines indicates the level of field nonuniformity

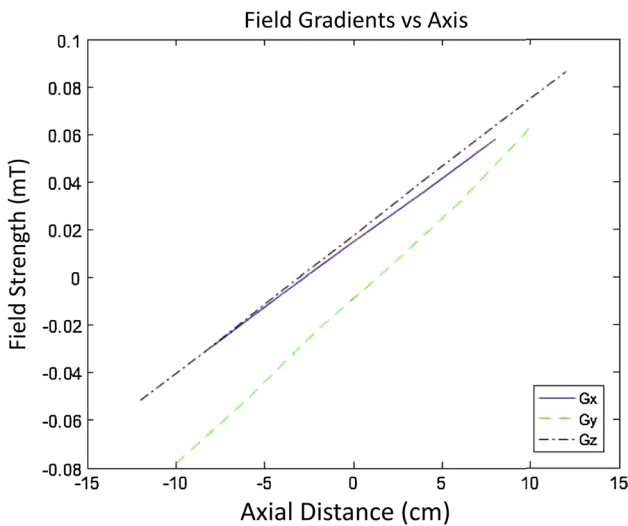


Fig. 5 Linearity of the X gradient (G_x), Y gradient (G_y), and Z gradient (G_z) magnetic fields. Slopes of the lines indicate gradient magnetic field strength

Linearity and uniformity of gradient magnetic fields

Similarly, magnetic field strengths generated by gradient coils were measured using the DSP 475 gaussmeter guided by the three-axis manipulator. Each gradient coil was

separately energized by supplying a steady current of 2.5 A using the XDL 35-5 T DC power supply, as above. Results for gradient field uniformity and linearity were analyzed using MATLAB and plotted in Figs. 4 and 5.

Imaging experiments

Imaging experiments of phantoms were carried out using the PMRI system. Two separate RF coils—transmit and receiver—were used. They were positioned cylindrically concentric to each other but with orthogonal magnetic fields. Imaging frequency was 113 kHz. The B_p field was 27 mT, and the strongest gradient was ~ 0.7 mT/m. To cover the FOV of 22 cm, RF bandwidth was chosen to be 7 kHz.

The pulse sequence used is shown in Fig. 6 and was controlled by the LabView code. The imaging process started by switching B_p on for 3.5 s, followed by an off state of 0.85 s during which image acquisition was done. The long B_p time was to take advantage of the relatively long T1 time of CSF [5]. Similarly, the relatively long time between B_p off and the $\pi/2$ pulse was to allow the inductive effects of B_p to fade out.

For the experiment shown in Fig. 7, repetition time was 4.35 s, number of phase-encoding steps 30, and number of slices one. Imaging time was 8.7 min. The figure also shows

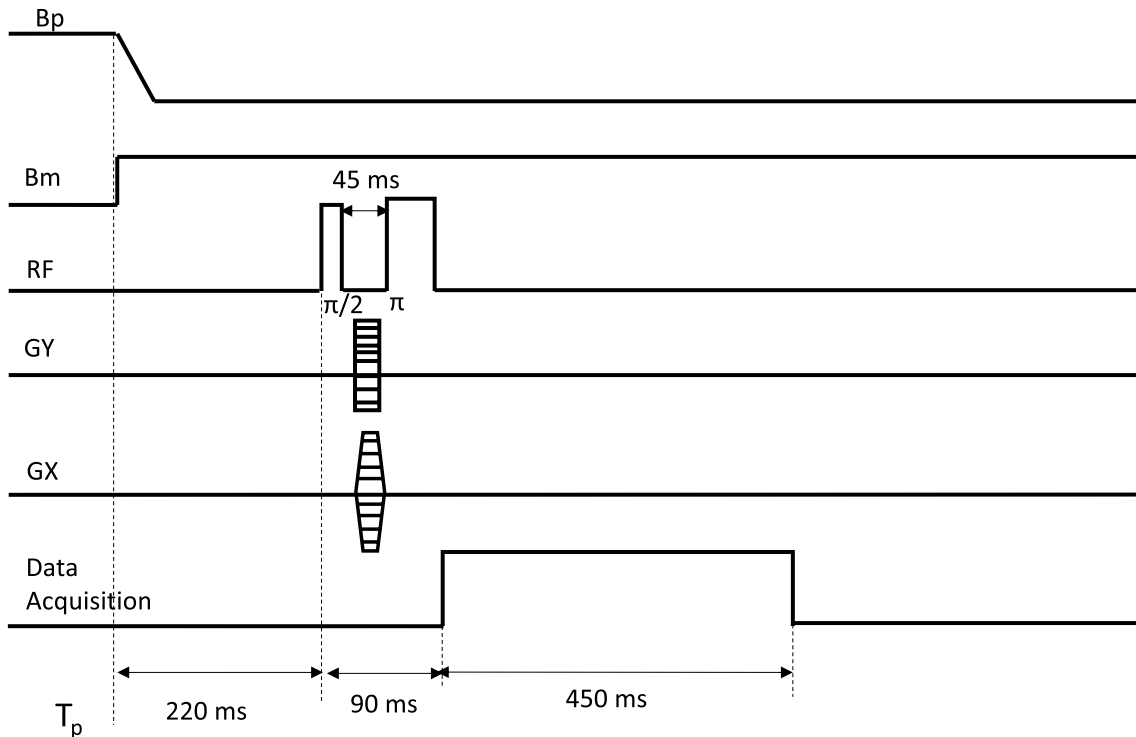


Fig. 6 Pulse sequence. $T_p = 3.5$ s, repetition time $T_R = 4.35$ s, echo time 90 ms, number of averages 4, number of phase encoding steps 30, acquisition frequency 113 kHz, pre-pulse field 27 mT, and imaging time 8.7 min

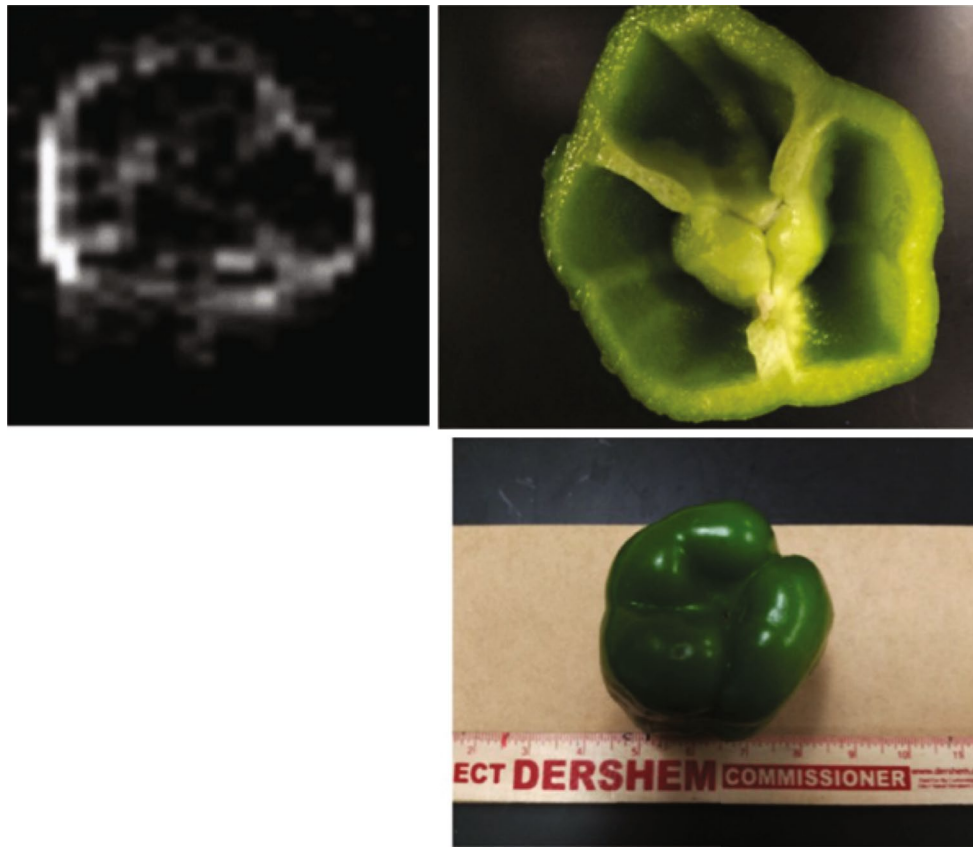


Fig. 7 Bell pepper image. Slice thickness 20 mm, and in-plane resolution 3 mm×3 mm

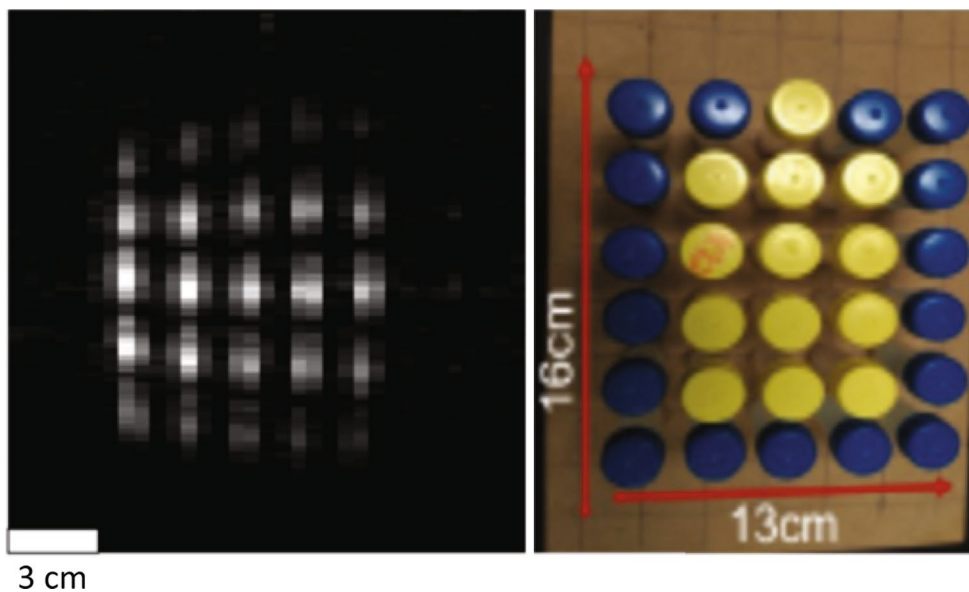
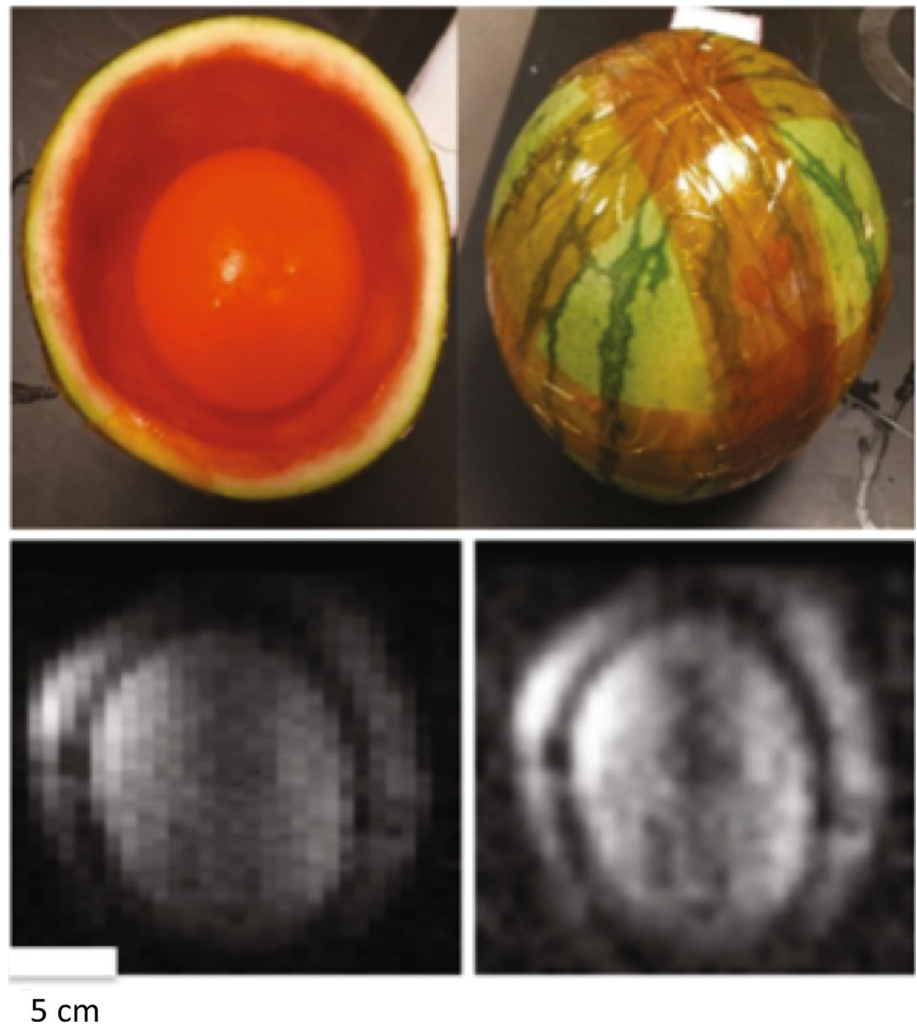


Fig. 8 Water tubes

photos of the imaged bell pepper. In one photo, the bell pepper was cut open to show the internal components, which correlate to what is seen in the image.

Figure 8 shows the image and photo of water bottles 10 mm in diameter and 15 mm in length. The bottles were filled with ordinary tap water without any paramagnetic

Fig. 9 Water melon image. The *bottom image* was partially processed using a MATLAB gaussian filter with standard deviation (SD) of 2



particles. Bottles were imaged using the following parameters: repetition time 4.35 s, number of phase-encoding steps 26, number of averages 10, number of slices one, and imaging time 18.85 min.

Figure 9 shows photos and images of a water melon that was cut into two and the inside flesh scooped out. A water-filled balloon was then inserted into the space, and the water melon was covered up and wrapped with Kapton tape. Imaging also followed the pulse sequence diagram shown in Fig. 6 with RT time of 4.35 s, number of averages 5, number of phase-encoding steps 26, and imaging time 9.5 min.

Discussion

Using phantom images, we demonstrated that a low-cost PMRI system can reach imaging resolutions sufficient for some less-demanding clinical applications, such as diagnosing hydrocephalus. It is our clinical judgement that hydrocephalus can be managed with an imaging slice thickness of

10 mm and in-plane resolution of $3\text{ mm} \times 3\text{ mm}$. We chose a design that can be assembled by hand using widely available materials and off-the-shelf electronics. Operating and maintaining such a system has far lower technical and infrastructure requirements compared with typical commercial imaging systems, which are essential for deploying this technology in many countries in the developing world.

The B_m magnetic field varied up to 5000 ppm within the FOV, with average field strength of 4 mT (Fig. 3). There is a slight departure from theoretical calculations in terms of absolute values of magnetic fields measured. Theoretical calculations are that a magnetic field of 0.83 mT/A and therefore a current of 4.721 A would give an average field strength of 3.94 mT. From COMSOL simulations (Fig. 1) mean field at the center was 3.875 mT and field uniformity over the 22-cm DSV was 0.13% (1300 ppm). Some deviation could be attributed to the imprecise positioning of coils as a result of hand winding. Kedzia et al. have shown that even slight changes in coil positioning can cause substantial distortions in magnetic field homogeneity [33]. Additionally,

kinks within the coil as a result of hand winding distort the directional flow of current and can create current loops, which further distort homogeneity of the magnetic field.

However, it is recommended that magnetic inhomogeneities should be smaller than the gradient magnetic field strength per voxel or pixel [22]. LF MRI image resolution of 2.5 mm × 3.5 mm has been shown to reveal considerable brain structure [34]. For diagnosis of hydrocephalus, we believe that a coarser in-plane resolution of 3 mm × 3 mm is adequate, because in the majority of cases, tissue contrast to reveal brain structure is not pertinent to treatment outcome. B_m field inhomogeneity in our experiment causes frequency shifts of 12 Hz over a 3-mm pixel. This implies that our gradient strengths should be >12 Hz per pixel, which is easily achieved with our gradient system.

Figure 4 shows contour plots of the X , Y , and Z magnetic field gradients, respectively. The contour lines in all cases are 10 μ T apart. Magnetic field uniformity is shown by how parallel the contour lines are while linearity is shown by how straight the contour lines are. We observe that gradient fields are fairly uniform but are linear within a limited range. Linearity of gradient fields is explored further by the line graphs in Fig. 5. Gradient strengths in the X , Y , and Z directions were calculated from the slopes of the graphs in Fig. 5 and were 542, 697, and 577 mT/m, respectively.

Considering the pixel size of 3 mm, these gradient fields give frequency shifts of 69, 89, and 74 Hz/pixel in the X , Y , and Z -directions, respectively. These frequency shifts caused by B_m inhomogeneity was only 17% of the weakest gradient strength and therefore permits successful imaging in our design.

From the images acquired (Figs. 7–9), distortions that are a reflection of the B_m field inhomogeneities and nonlinearities can be inferred. In the larger sample images (Figs. 7 and 9), a loss of signal can be seen towards the edges of the images. This could be due to a number of factors. The RF transmitter coil is comparable in length to the dimensions of the samples being imaged. Ginsberg and Melchner found that a saddle coil gives the most uniform field when coil length is twice its diameter [35]. When dealing with large-volume coils, it becomes difficult to adhere to these dimensions, as the saddles could be unnecessarily long. Our saddle coil has a length-to-diameter ratio of 1.2. The RF magnetic field is therefore not uniform throughout the imaging volume. Simulations suggest that the usable volume of a saddle RF coil is that region where the magnetic field is uniform to within 15% [36]. RF field inhomogeneities toward the edges of the coil lead to loss of signal. Similar to the transmitter coil, the receive coil has dimensions comparable with those of the samples. Additionally, the gradient magnetic fields are more uniform at the center of the coil system, with nonuniformities at the outer edges, as seen from Figs. 7–9. This can result in spin dephasing at the edges. We also see

a brightening of the images on the left side, which could be caused by proximity of the samples to the RF shield inserted into the imaging volume. The RF shield can produce nonuniform concentration of RF signal, causing brightness that would be visible in the images. Distortions in the image of the water bottles could be caused by gradient nonlinearities, as the contour plots shown in Fig. 4.

Furthermore, magnetic field instabilities caused by the B_p switching can cause spin dephasing, which can be more pronounced at the edges of the samples where the nonuniformity may be greater. This dephasing causes signal loss that can affect image contrast, making it difficult to define boundaries between different structures. The images acquired were of samples with high water content. Water is known to have long longitudinal relaxation times (T_1) [37] and therefore our delay time of 220 ms before application of the $\pi/2$ pulse was still appropriate. However, human tissues have relatively short T_1 relaxation times close to 200 ms especially at low magnetic fields [14]. We are working toward reducing the delay time by improving B_p switching. Nevertheless, imaging can be done for maximum contrast of CSF, which is particularly relevant to hydrocephalus diagnostics.

Conclusions

Coil designs and construction used in the PMRI system described here were based on general procedures proposed and described by many researchers [22, 23, 28, 30, 38]. The fact that we were able to acquire usable images with B_m magnetic field inhomogeneities of up to 5000 ppm in an unshielded room is testament to the robustness of the PMRI technology and an indication of its suitability for applications in developing countries. The SNR of the system can be greatly improved by increasing the B_m magnetic field until coil noise is dominated by sample (tissue) Johnson noise [11]. This, however, needs to be done carefully, as increasing the strength of B_m would substantially increase the power requirement of the system. Despite the imperfections seen in such a simple device, images acquired show the potential functionality of the system for our intended first application in infant hydrocephalus. The fact that the system was assembled by hand shows the robustness of its ease of construction, which makes it straightforward to replicate and scale in developing countries. The system was operated at a B_m of 2.66 mT and a B_p of 27 mT, with power consumption of 140 and 410 W, respectively. At this low power, the in-plane resolution of 3 mm × 3 mm is adequate for treatment decisions in hydrocephalic cases where the primary need is to distinguish between CSF and brain tissue. For deployment in Africa, we have embarked on a program to automatically compensate for field imperfections, optimize transmit–receive coil specifications, achieve adequate

thermal and electrical safety specifications, and optimize a variety of image acquisition algorithms to further improve spatial resolution and contrast. Redesigning such a system for adult head imaging will be a straightforward extension of this effort.

Acknowledgements This work was funded by the Endowment funds of Harvey F. Brush at Penn State University, US Department of Energy Los Alamos National Laboratory Directed Research and Development program (IMS), and US National Institutes of Health Director's Pioneer Award 5DP1HD086071 (SJS).

Authors contributions JO: Responsible for winding magnet coils and carrying out imaging experiments. JRH: Responsible for solid work Computer Aided Designs (CAD) of the magnet and coil systems and for image analysis. SC: Responsible for theoretical analysis of magnetic field uniformity for the designs. ST: Participated in designing and building radio frequency amplifiers. TN: Participated in radio frequency tuning of coils, and contributed to image analysis. IMS: Consulted on all aspects of device design, wrote the labview program used in imaging, and helped carry out imaging experiments. SJS: Overall supervisor for the concept, design, implementation, and analysis for the project.

Compliance with ethical standards

Conflict of interest Author IMS has received research support from the US Los Alamos National Laboratory's Laboratory Directed Research and Development program. Author SJS has received support from the Endowment funds of Harvey F. Brush at Penn State University, and from the US NIH National Institutes of Health Director's Pioneer Award Grant 5DP1HD086071.

Ethical standard The study was conducted under the scientific ethics guidelines of The Pennsylvania State University, and in accordance with the use of US NIH funding. There were no human or animal research subjects. No study advertising was made and no remuneration was offered.

References

- Kahle KT, Kulkarni AV, Limbrick DD Jr, Warf BC (2016) Hydrocephalus in children. *Lancet* 387(10020):788–799
- Warf BC (2005) Hydrocephalus in Uganda: the predominance of infectious origin and primary management with endoscopic third ventriculostomy. *J Neurosurg* 102(1 Suppl):1–15
- Warf BC, Alkire BC, Bhai S, Hughes C, Schiff SJ, Vincent JR, Meara JG (2011) Costs and benefits of neurosurgical intervention for infant hydrocephalus in sub-Saharan Africa. *J Neurosurg Pediatr* 8(5):509–521
- Kulkarni AV, Schiff SJ, Mbabazi-Kabachelor E, Mugamba J, Ssenyonga P, Donnelly R, Levenbach J, Monga V, Peterson M, MacDonald M, Cherukuri V, Warf BC (2017) Endoscopic treatment versus shunting for infant hydrocephalus in Uganda. *N Engl J Med* 377(25):2456–2464
- Rooney WD, Johnson G, Li X, Cohen ER, Kim SG, Ugurbil K, Springer CS Jr (2007) Magnetic field and tissue dependencies of human brain longitudinal $1\text{H}_2\text{O}$ relaxation in vivo. *Magn Reson Med* 57:308–318
- Klein H-M (2016) clinical low field strength magnetic resonance imaging: a practical guide to accessible MRI. Springer, New York
- Muhogora WE et al (2010) Paediatric CT examinations in 19 developing countries: frequency and radiation dose. *Radiat Prot Dosim* 140(1):49–58
- Brenner DJ, Hall EJ (2007) Computed tomography—an increasing source of radiation exposure. *N Engl J Med* 357(22):2277–2284
- Sepponen RE, Sipponen JT, Sivula A (1985) Low field (0.02 T) nuclear magnetic resonance imaging of the brain. *J Comput Assist Tomogr* 9(2):237–241
- Nascimento GCD, Engelsberg M, Souza RED (1992) Digital NMR imaging system for ultralow magnetic fields. *Meas Sci Technol* 3(4):370–374
- Macovski A, Conolly S (1993) Novel approaches to low-cost MRI. *Magn Reson Med* 30(2):221–230
- Matter NI, Scott GC, Grafendorfer T, Macovski A, Conolly SM (2006) Rapid polarizing field cycling in magnetic resonance imaging. *IEEE Trans Med Imaging* 25(1):84–93
- Savukov I, Karaulanov T, Castro A, Volegov P, Matlashov A, Urbatis A, Gomez J, Espy M (2011) Non-cryogenic anatomical imaging in ultra-low field regime: hand MRI demonstration. *J Magn Reson* 211:1–23. <https://doi.org/10.1016/j.jmr.2011.05.011>
- Savukov MI, Karaulanov T (2013) Magnetic-resonance imaging of the human brain with an atomic magnetometer. *Appl Phys Lett* 103:1–4
- Lothar S, Schiff SJ, Neuberger T, Jakob PM, Fidler F (2016) Design of a mobile, homogeneous, and efficient electromagnet with a large field of view for neonatal low-field MRI. *Magn Reson Mater Phy* 29:1–8
- Sarracanie M, LaPierre CD, Salameh N, Waddington DEJ, Witzel T, Rosen MS (2015) Low-cost high-performance MRI *Sci Rep* 5:15177
- Halbach K (1980) Design of permanent multipole magnets with oriented rare earth cobalt material. *Nucl Instrum Methods* 169:1–10
- Kimura T, Geya Y, Terada Y, Kose K, Haishi T, Gemma H, Sekozawa Y (2011) Development of a mobile magnetic resonance imaging system for outdoor tree measurements. *Rev Sci Instrum* 82(5):053704
- Kose K, Haishi T (2011) High resolution NMR imaging using a high field yokeless permanent magnet. *Magn Reson Med Sci* 10:159–167
- Cooley CZ, Stockmann JP, Armstrong BD, Sarracanie M, Lev MH, Rosen MS, Wald LL (2015) Two-dimensional imaging in a lightweight portable MRI scanner without gradient coils. *Magn Reson Med* 73(2):872–883
- Blümler P, Casanova F (2016) Hardware developments: Halbach magnet arrays. In: Johns ML, Fridjonsson EO, Vogt SJ, Haber A, Price W (eds) *Mobile NMR and MRI: developments and applications*. The Royal Society of Chemistry, Cambridge, pp 133–157
- Morgan P, Conolly S, Scott G, Macovski A (1996) A readout magnet for prepolarized MRI. *Magn Reson Med* 36(4):527–536
- Kirschvink JL (1992) Uniform magnetic-fields and double-wrapped coil systems—improved techniques for the design of bioelectromagnetic experiments. *Bioelectromagnetics* 13(5):401–411
- Merritt R, Purcell C, Stroink G (1983) Uniform magnetic field produced by three, four, and five square coils. *Rev Sci Instrum* 54(7):879–882
- Rubens SM (1945) Cube-surface coil for producing a uniform magnetic field. *Rev Sci Instrum* 16(9):243–245
- Gottardi G, Mesirca P, Agostini C, Remondin D, Bersani F (2003) A Four coil exposure system (tetracoil) producing a highly uniform magnetic field. *Bioelectromagnetics* 24(2):125–133
- Wire industries MWS. World's largest selection of specialty magnet wire. Available at: http://www.mwswire.com/pdf_files/mws_tech_book/techbook2016.pdf. Accessed 4 Apr 2018

28. Hidalgo TS (2010) Theory of gradient coil design methods for magnetic resonance imaging. *Concepts Magn Reson Part A* 36A(4):223–242
29. Golay MJE (1958) Field homogenizing coils for nuclear spin resonance instrumentation. *Rev Sci Instrum* 29(4):313–315
30. Hoult DI (1978) The NMR receiver: a description and analysis of design. *Prog Nucl Magn Reson Spectrosc* 12(1):41–77
31. Henry OW (2009) *Electromagnetic compatibility engineering*. John Wiley & Sons, New York
32. Schulz RB, Huang GC, Williams WL (1968) RF shielding design. *IEEE Trans Electromagn Compat EMC-10*(1):168–175. <https://doi.org/10.1109/TEMC.1968.302925>
33. Kedzia P, Czechowski T, Baranowski M, Jurga J, Szcześniak E (2013) Analysis of uniformity of magnetic field generated by the two-pair coil system. *Appl Magn Reson* 44(5):605–618
34. Sarracanie M et al (2015) Low-cost high-performance MRI. *Sci Rep* 5:15177
35. Ginsberg DM, Melchner MJ (1970) Optimum geometry of saddle shaped coils for generating a uniform magnetic field. *Rev Sci Instrum* 41(1):122–123
36. Samila A (2015) Simulation of magnetic field topology in a saddle-shaped coil of nuclear quadrupole resonance spectrometer. *Prog Electromagn Res Lett* 56:67–73
37. Hinshaw WS, Bottomley PA, Holland GN (1977) Radiographic thin-section image of the human wrist by nuclear magnetic resonance. *Nature* 270(5639):722–723
38. Rashid SA, Amiruddin BS, Chew TH (2008) Magnetic field simulation of Golay coil. *J Fundam Sci* 4:353–361